Carbon nanotube@manganese oxide nanosheet core-shell structure encapsulated within reduced graphene oxide film for flexible all-solid-state asymmetric supercapacitors

Shuxing Wu [a], Kwan San Hui [b,*], Kwun Nam Hui [a,*]

[a] Institute of Applied Physics and Materials Engineering, University of Macau, Avenida da Universidade, Macau, China

[b] School of Mathematics, University of East Anglia, Norwich, NR4 7TJ, United Kingdom

*Corresponding author:

E-mail: k.hui@uea.ac.uk (Kwan San Hui)

E-mail: bizhui@umac.mo (Kwun Nam Hui)

ABSTRACT

To achieve flexible energy storage devices with high performance, a new class of flexible electrodes with exquisite architectures that provide well-defined pathways for efficient ionic and electronic transport is highly needed. A flexible 3D electrode is fabricated based on assembling 1D carbon nanotube@manganese oxide (MnO_2) nanosheet core-shell structures (CM) with 2D reduced graphene oxide (rGO) nanosheets. MnO_2 nanosheets are grafted vertically along the carbon nanotube backbone through a secondary (seeded) growth. Flexible hybrid films (GCM) composed of CM and rGO are prepared by vacuum filtration of the mixed dispersions of both components assisted by electrostatic interactions. By adopting this ternary hybrid architecture, the GCM electrode exhibits exceptional charge storage capability in 1 M Na_2SO_4 aqueous electrolyte with high specific capacitance (298 F g^{-1} at 0.5 A g^{-1}), good rate capability, and high cycling stability (90.3% retention over 5000 cycles). A highly flexible all-solid-state asymmetrical supercapacitor is assembled with GCM as the positive electrode and holey graphene film spaced with carbon sphere (H-GCS) as the negative electrode. GCM//H-GCS asymmetric supercapacitor delivers a maximum energy density of 24.6 Wh kg^{-1} and a power density of 9005.3 W kg^{-1} with excellent cycle life of 75.9% retention after 10 000 cycles.

1. Introduction

The growing market for flexible and bendable electronics, such as roll-up screens, portable devices, flexible sensors, and wearable devices has stimulated rapid development in flexible energy storage devices. Flexible supercapacitors attract extensive attention due to their high power density, fast charge/discharge rate, long cycle life, and lightweight. Nevertheless, the limited energy density (1–10 Wh kg^{-1}) limits the wide applications of these supercapacitors [1]. Asymmetric electrode configurations, which include coupling different positive and negative electrode materials that can be charged/discharged in well-separated potential windows in the same electrolyte, offer the best trade-off between high energy and power densities. In this regard, well-designed architectures with nanostructured carbonaceous matrixes and pseudocapacitive materials are critical to the success of this technology [2].

RuO_2 and MnO_2 are typical pseudocapacitive materials instead of battery-type redox active materials [3, 4]. RuO_2 has a high specific capacitance of 740 F g^{-1} in acidic electrolyte due to its high electrical conductivity (10^5 S cm^{-1}) and pseudocapacitance with protons [5]. However, commercial application of RuO_2-based supercapacitors is limited by the high cost and environmental harmfulness of Ru. Since the first report on the pseudocapacitive behavior of MnO_2 by Goodenough et al. in 1991, MnO_2 has become an attractive material for supercapacitors [6, 7]. The theoretical pseudocapacitance of MnO_2 is approximately 1370 F g^{-1} [8]. Unlike RuO_2-based strong acid systems, MnO_2 functions well in neutral aqueous electrolytes, thereby demonstrating its high environmental friendliness and safety [9]. Moreover, MnO_2 has attracted tremendous attention as a promising candidate for electrode material because of its low cost, natural

abundance, non-toxicity, and good chemical stability [10, 11]. As such, MnO_2 is an excellent cost-effective alternative to RuO_2 for supercapacitors application. However, its poor electrical conductivity (10^{-5} S cm^{-1} to 10^{-6} S cm^{-1}) and low ion diffusion constant significantly limit its energy storage capacity. A promising strategy for incorporating carbonaceous nanomaterials into MnO_2 electrode materials has been applied to address these bottleneck issues. MnO_2 and carbon nanotube (CNT) are among the highly studied cathode systems for asymmetric supercapacitors because of the outstanding electrical conductivity and large surface area of CNT [12, 13]. CNT could serve as a cushion to support MnO_2, thus providing high electron collection efficiency, efficient electrolyte ion transport, accessible electroactive site, and improved cycling stability. Nevertheless, as-developed CNT/MnO_2 hybrid electrodes still suffer from several draw backs: (i) the MnO_2 is coated on the outer surface of CNT; hence, the poor conductivity of the MnO_2 is not effectively improved [14, 15]; (ii) the CNT/MnO_2 hybrid is sensitive to mechanical detachment/deformation during folding and twisting; and (iii) the inevitable dissolution of MnO_2 into the electrolyte.

We report a free-standing and flexible reduced graphene oxide (rGO)/CNT/MnO_2 ternary hybrid film (GCM) in this work. Scheme 1 shows the schematic of the fabrication process. CNT@MnO_2 core-shell structure (CM) was first synthesized through secondary (seeded) growth and then functionalized with poly(diallyldimethylammonium) (PDDA) to become positively charged. A negatively charged rGO colloid was prepared through chemical reduction of graphene oxide. With the assistance of electrostatic self-assembly, 1D CM nanowires and 2D rGO nanosheets were integrated to construct a robust 3D hybrid structure via a simple vacuum filtration method. The unique design and

fabrication of the hybrid architecture have the following advantages: (I) the vertically grown MnO_2 nanosheets surface on the CNT provides numerous channels for electrolyte ion diffusion and electrons transport, simultaneously reduces the structural collapse, and prevents aggregation of MnO_2 nanosheets; (II) rGO nanosheets provide fertile opportunities for constructing of graphene-based structures with high mechanical flexibility; (III) CM significantly improves capacitive performances due to its pseudocapacitive contribution and functions as a spacer to prevent aggregation and restacking of the rGO nanosheets; and (IV) the electrostatic interactions improve the interfacial binding force between the CM and rGO nanosheets, which prevent the dissolution of MnO_2 active material into the electrolyte. The GCM electrodes delivered a high specific capacitance of 298 F g^{-1} at 0.5 A g^{-1} in the 1 M Na_2SO_4 aqueous electrolyte and high cycling stability (90.3% retention over 5000 cycles). A flexible all-solid-state asymmetrical supercapacitor (FASCs) with GCM as the positive electrode and carbon spheres pillared holey graphene (H-GCS) [16] as the negative electrode and a potassium polyacrylate (PAAK)/KCl gel electrolyte, was assembled. The as-fabricated device operated reversibly in the voltage range of 0–1.8 V, and exhibited enhanced energy storage and power delivery (a maximum energy density of 24.6 Wh kg^{-1} and power density of 9005.3 W kg^{-1}) and outstanding cycling stability.

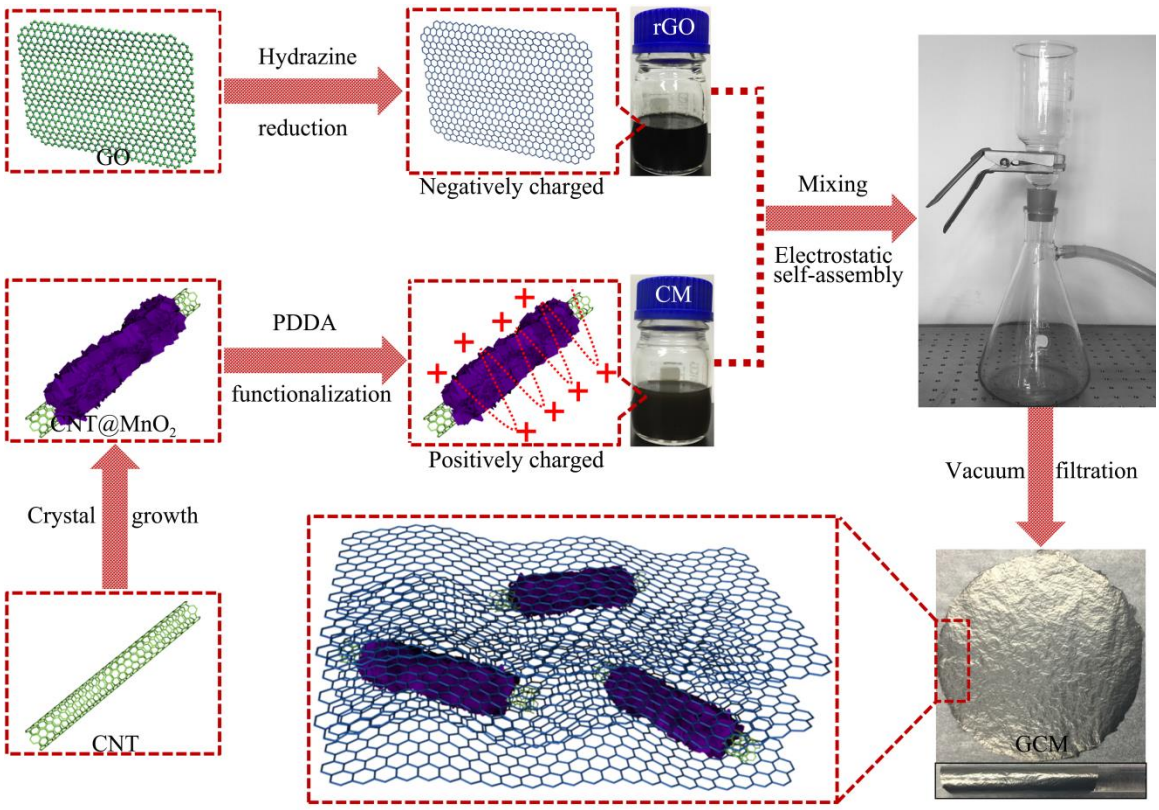

Scheme1. Schematic illustration of the fabrication process of GCM film.

2. Experimental

2.1 Materials

GO was used for the preparation by a modified Hummers' method [17, 18]. Multi-walled carbon nanotubes (MWCNTs) was purchased from Iljin Nanotech Co., Ltd (purity: > 95%, length: 10~15μm, diameter: 10~30 nm). PAAK, potassium chloride, poly(diallyldimethylammonium) (PDDA, typical Mw of 100 000−200 000, 25% aqueous solution), and sodium sulfate were used as received from Sigma-Aldrich.

2.2 Preparation of GCM film

Stable aqueous CNT dispersions at a concentration of 4 mg/mL were prepared by tip sonication. MnO_2 nanosheets were grown on CNTs through a simple hydrothermal method. $KMnO_4$ (0.075 M) was added into the as-prepared CNT dispersion with constant stirring at room temperature (RT) for 6 h. Subsequently, the mixture was sealed in a 50 mL Teflon-lined stainless steel autoclave and kept in an oven at 150 °C for 5 h. After the hydrothermal treatment, the red-brown products were obtained through vacuum filtration, water washing and drying process. Positively charged CM was prepared through PDDA-functionalization. 100 mg of CM was dissolved in 100 mL of deionized (DI) water containing 0.5 mg of PDDA. The resulting dispersion was stirred at RT for 6 h. The PDDA-functionalized CM was centrifuged, filtrated and rinsed with DI water. The dried functionalized CM at different weight ratios was ultrasonically re-dispersed in 50 mL of water with the pH adjusted to 11 using a diluted ammonia solution. Negatively charged rGO colloid was prepared via chemical reduction according to the previous report [19]. With the assistant of electrostatic interactions, freestanding and flexible GCM was fabrication by filtering the mixture the positively charged CM aqueous solution with negatively charged rGO colloid over a polytetrafluoroethylene membrane (0.2 μm pore size, 47 mm in diameter; SciLab), followed by water washing, and peeling off from the filter membrane.

2.3 Preparation of H-GCS film

Carbon spheres (CSs) were synthesized by a classical hydrothermal carbonization method [20]. Positively charged CSs were functionalized with cetyltrimethylammonium (CATB). In a typical process, the as-prepared CSs powder was dispersed into CTAB solution (1 wt%). The resulting dispersion was stirred for 5 h and excess CTAB was removed by

washing with water. Functionalized CSs aqueous dispersion was added into rGO colloid. After 2 h, a thin film was formed by using vacuum filtration of the mixture. Porous structures were obtained through KOH etching [16].

2.4 Fabrication of flexible all-solid-state supercapacitor

The all-solid-state asymmetric supercapacitors were assembled with the GCM as the positive electrode and H-GCS as the negative electrode with PAAK/KCl gel as a solid electrolyte. In order to balance the charge between the two electrodes, the area ratio of H-GCS electrode and GCM electrode was fixed to be 4:1. In the assembly of GCM//H-GCS flexible asymmetric devices, the areas of H-GCS electrode (negative) and GCM electrode (positive) are 2 cm × 2 cm and 1 cm × 1 cm, respectively. The mass loading of GCM and H-GCS is 1.08 mg and 1.88 mg, respectively, while the area density of GCM and H-GCS is 1.08 mg cm^{-2} and 0.47 mg cm^{-2}, respectively. Gold coated polyethylene terephthalate (PET) membranes were used as conductive plates. The PAAK/KCl electrolyte was prepared as follows: PAAK (3.0 g) and KCl (3.0 g) were dissolved in 30 mL water with vigorous and continuous stirring at 85 °C until the solution become clear [21]. Prior to the assembling, both electrodes were soaked in the PAAK/KCl sol for 5 min and then allowed to solidify at RT for 6 h. Finally, they were assembled together under pressing and kept at 45 °C for 12 h to remove excess water.

2.5 Characterization

The characterizations of both structure and morphology were performed by XRD (Rigaku MPA-2000), Raman spectrometer (Jobin-Yvon Horiba HR800, 514 nm), XPS (Thermo VG Escalab 250), AFM (Nanoscope IIIa Multimode, Digital Instruments, California),

SEM (Hitachi, S-4800), TEM (FEI Talos, USA). Electrochemical measurements including cyclic voltammetry (CV), galvanostatic charge/discharge (GCD), and electrochemical impedance spectroscopy were conducted in the range from 10 m Hz to 1 M Hz with an electrochemical station (IviumNstat). A three-electrode system, with a Pt counter electrode, a SCE reference electrode and a 1.0 M $NaSO_4$ aqueous electrolyte, was used to test the electrochemical performance of individual electrodes. The specific capacitance (Cs) of the individual electrode derived from GCD tests was calculated from the following equation of $Cs = I\Delta t/m\Delta V$, where Cs ($F\ g^{-1}$), I (A), Δt (s), ΔV (V), and m (g) are the specific capacitance, discharge current, discharge time, potential window, and mass of the individual electrode, respectively. The performances of the asymmetric supercapacitors were measured using a two-electrode configuration. Energy density (E, Wh kg^{-1}) and power density (P, W kg^{-1}) of the devices were calculated using the following equations of $C_t = I\Delta t/M\Delta V$, $E = 1/2C_t\Delta V^2$, and $P = E/\Delta t$, where C_t ($F\ g^{-1}$) is the gravimetric capacitance of the devices and M (g) is the total mass of the film electrodes.

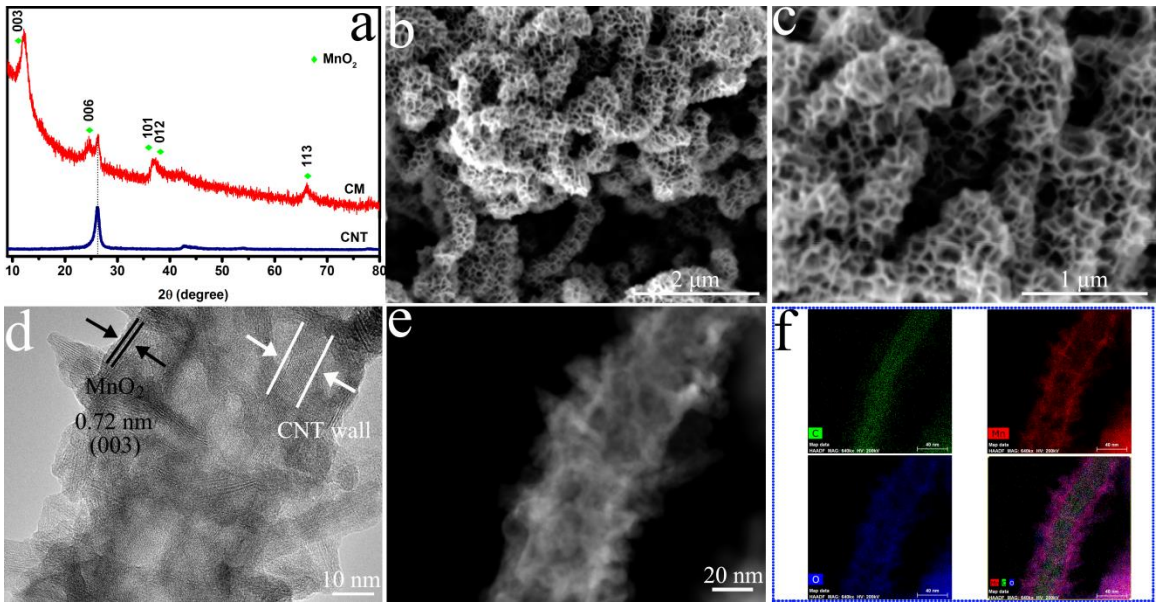

Fig. 1. (a) XRD patterns of CNT and CM; (b and c) SEM images at different magnifications of CM; (d) TEM image of CM; (e) HAADF-STEM and (f) EDS mapping of C, O, and Mn elements on an individual CM core-shell structure.

3. Results and discussion

Unlike previous reports on the synthesis of CNT/MnO_2 nanocomposites, CM was obtained using a secondary (seeded) growth procedure. First, when the CNT suspension was mixed with $KMnO_4$, the CNT and MnO_4^- experienced a slow redox reaction and produced MnO_2 nanocrystals according to the following equation [22]:

$$4MnO_4^- + 3C + H_2O \leftrightarrow 4MnO_2 + CO_3^{2-} + 2HCO_3^- \quad (1)$$

The CNT is a good electronic conductor and serve as the reductant in the redox process. The electron transfer from CNT to $KMnO_4$ (used the oxidant) upon direct contact lead to the reduction of $KMnO_4$ and caused it to deposit nanocrystalline MnO_2 onto the CNT surface. The initiation of the reaction (1) can be attributed to the CNT defect and/or tube end [22]. The CNTs used in our work were curved, and their curved appearance suggested high concentration of defects in the structure [23]. When the purple solution was treated under controlled conditions, MnO_2 nanosheets were formed on the CNTs, which can be formulated as [24, 25]:

$$4KMnO_4 + 2H_2O \leftrightarrow 4MnO_2 + 4KOH + 3O_2 \quad (2)$$

During the hydrothermal reaction, new MnO_2 nuclei were formed and the preformed MnO_2 nanocrystallines acted as heterogeneous nucleation sites for the second

crystallization. The self-assembly of the MnO_2 nuclei lead to the generation of nanosheets and the interlaced accumulation of MnO_2 nanosheets restricts the growth by each other, forming an alveolate-like structure [26]. The XRD patterns of the pure CNT and CM are shown in Fig.1a. The five peaks of the CM were observed at 2Θ values of 12.32°, 24.78°, 36.63°, 37.36°, and 66.91°, corresponding to the crystal planes of (003), (006), (101), (012), and (113) in birnessite-type MnO_2, respectively, with a rhombohedral lattice (a = 2.849 Å, c = 21.53 Å) and a $R\bar{3}m$ symmetric group (JCPDS 86-0666). Birnessite is a 2D octahedral layer structure, comprising edge-shared MnO_6 octahedral layers that form a tunnel/interlayer spacing of approximately 7 Å. Moreover, K^+ cations and water molecules were in the facade of the oxygen trigonal prism offered by the oxygen atoms in the MnO_6 layer [25, 27]. In the XRD analysis, the peak at 12.32 ° with d = 7.2 Å suggested the presence of the birnessite octahedral layer structure with K^+ cations in the interlayer space [27]. An additional peak at 26.3° in the XRD pattern of the CM attributed to the (002) plane of the hexagonal graphite structure implies the presence of CNTs [28]. Fig. 1b and c show the SEM images of CM. After the hydrothermal reaction, a uniform and dense coating of MnO_2 nanosheets was produced on the individual CNT surface (Fig. 1b). No aggregation of MnO_2 particles off the CNT support was observed. The enlarged view (Fig. 1c) shows that the curved nanosheets are in mutual contact and might form an excellent conductive network that is not easily detached from the CNT core. The vertically aligned nanosheets are interconnected with one another to create an open and porous structure. This unique structure can provide more active sites that are in contact with electrolyte ions and allow easy access for electrolyte ions into the electrolyte/electrode interface [29]. The energy dispersive X-ray spectrometer (EDS) line,

which scans across the nanowire, confirmed the core-shell configuration of CM (Fig. S1). The morphology and microstructure of CM were further investigated using TEM. The MnO_2 nanosheets were intimately grafted throughout the longitudinal axis of the nanotube. The core-shell structure might give high mechanical strength, thereby maintaining its structural integrity while against the mechanical deformation (Fig. 1d). The interplanar spacing in the internal core was 3.4 Å, which was consistent with the spacing of the (002) planes of CNT. Moreover, the high resolution TEM characterization shows the (003) lattice of birnessite MnO_2 (d = 7.2 Å), which corresponds well to the XRD data in Fig. 1a. The typical high-angle annular dark-field scanning TEM (HAADF-STEM) image of an individual CM hybrid structure and the corresponding EDS mapping analysis (Fig. 1e, f) clearly confirmed the well-defined core-shell structure with a CNT core and MnO_2 nanosheets. The HAADF-STEM shows a uniform distribution of the elements Mn, C, and O and clearer identification of atomic core-shell architecture can be observed through the overlapped Mn, C, and O mapping images.

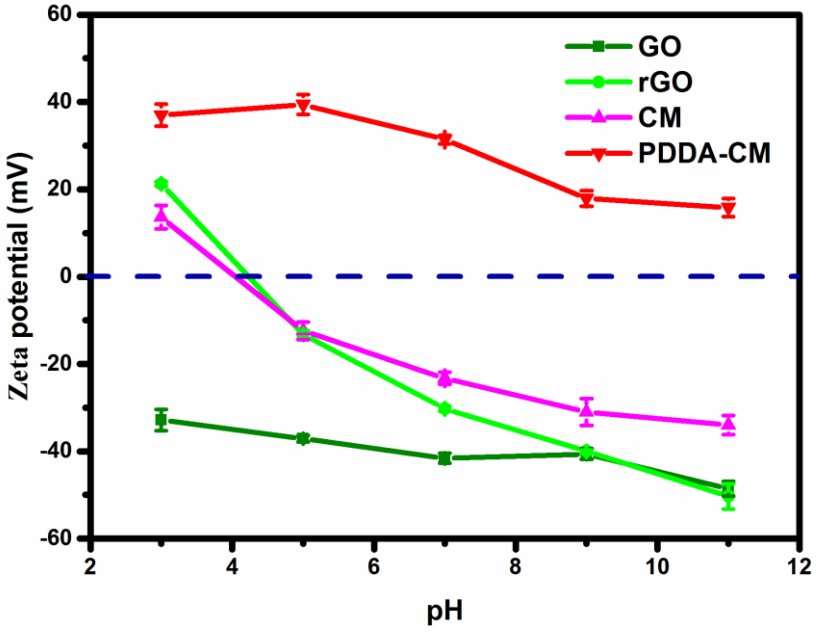

Fig. 2. (a) Zeta-potential profiles of GO, rGO, and CM before and after functionalization with PDDA.

The GCM films were fabricated *via* the Coulombic self-assembly of rGO colloid and CM, followed by a simple vacuum filtration process. Fig. 2 shows the zeta-potentials of GO, rGO, and CM before and after PDDA functionalization in water as a function of pH. The GO dispersion constantly displayed negative potentials with pH varying from 3–11 due to the ionization of carboxylic acid and phenolic hydroxyl groups on the GO sheets (Fig S2) [19, 30, 31]. The zeta-potential of the rGO dispersion reduced by hydrazine remained positive before reaching an isoelectric point at pH 4–5. The negative zeta-potential in pH 5–11can be attributed to the ionization of the partial oxygen functional groups that were incompletely reduced [19]. The zeta-potential of CM is below zero when the pH value exceeded 4. After functionalization with the cationic polyelectrolyte PDDA, the zeta-

potential of the CM consistently displayed a positive zeta-potential at pH 3–11, thereby indicating successful functionalization with the cationic polyelectrolyte. Within the paradigm of colloidal chemistry, the final rGO deposition morphologies largely rely on the pH of colloidal dispersions [32]. At high pH, a single-layer can be preserved because of the electrostatic repulsion originating from the negatively charged functional group [33]. At pH 11, the positively charged PDDA-CM and the negatively charged rGO formed electrostatic interactions, thereby driving the co-assembly of rGO and CM.

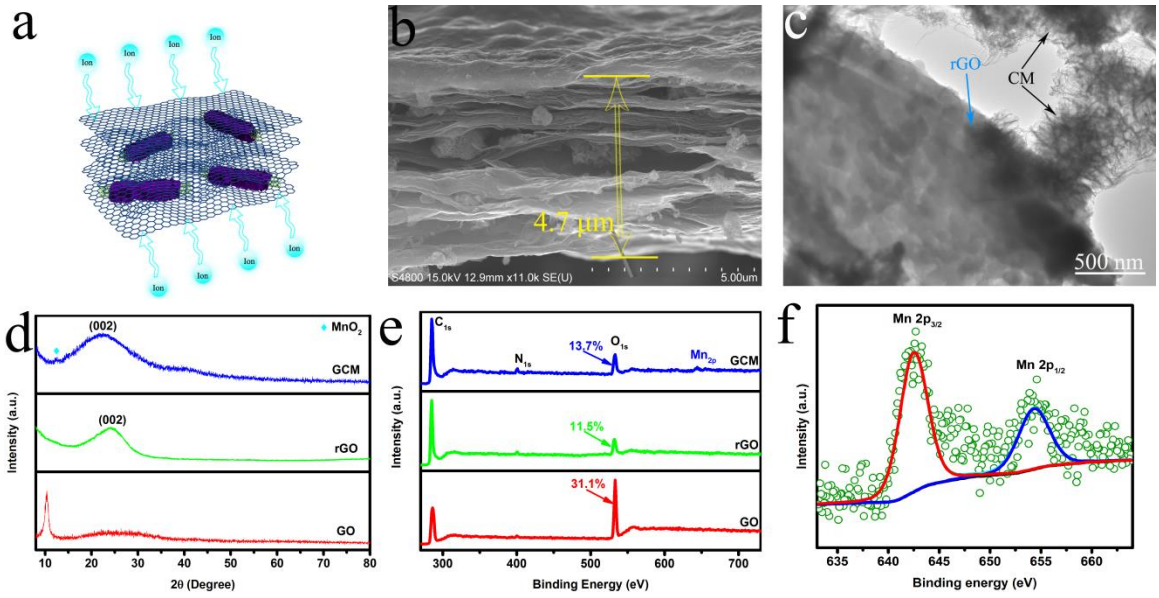

Fig. 3. Schematic illustration (a), Cross-sectional SEM images (b), and TEM image (c) of GCM thin films; XRD patterns (d) and XPS survey spectra (e) of GO, rGO, and GCM, and (f) Mn 2p XPS spectrum.

After shaped to thin films, freestanding GCM hybrid films were obtained. Fig. S3 shows the digital photographs of freestanding rGO and GCM films. Numerous CM structures were embedded among rGO sheets; however, the freestanding GCM thin films remained

highly flexible. Similar to rGO films, the GCM films can be easily wrapped around glass rods without noticeable structural damage. Fig. 3a and 3b show the illustration and cross-section SEM images of the GCM film. Evidently, in pure rGO film, the graphene nanosheets are restacked together in the pure rGO film (Fig. S4), whereas in the GCM film, the rGO layers were separated apart by CM and the inter-layer space between rGO layers became observed. The thickness of CM increased to 4.7 μm, compared with the 2.3 μm in rGO film. This sandwich structure facilitates the electrolyte ion diffusion between rGO layers and affords additional electron transport channels and mechanical protection for a fast, complete, and sustainable redox reaction of MnO_2. The sandwich structure was further demonstrated by TEM image, in which the CM structure was embedded in the skeleton of the 3D graphene framework and wrapped by rGO layers (Fig. 3c).

XRD and XPS were used to characterize the composites. The XRD patterns for the GO powder, rGO film, and GCM film are included for comparison in Fig. 3d. A typical peak near 10.3° was observed for the GO powder, which suggested decent crystallinity of the aligned GO layers along their stacks and increased *d*-spacing (~8.6 Å) due to the presence of oxygen-containing functional groups and intercalated H_2O molecules [34]. In the rGO films, a broad and weak peak at *ca.* 24° can be indexed to the (002) reflections of graphitic carbon, indicating the poor ordering of rGO sheets along their stacking direction [35]. Moreover, characteristic peaks of rGO and birnessite-type MnO_2 can be observed in the XRD pattern of GCM. The (002) peak position of GCM shifted to a lower degree than that of the rGO film, indicating that the CMs are well encapsulated within the rGO nanosheets [16]. Fig. 3e shows the full XPS spectra of the GO powder, rGO film, and

GCM film. The surface oxygen groups in the GO, rGO, and GCM were 31.1%, 11.5%, and 13.7%, respectively. Mn existed only in the spectrum of GCM and the Mn 2p3/2 and Mn 2p1/2 peaks were located at 642.5 and 654.3 eV, indicating the presence of Mn^{4+} in the sample (Fig. 3f).

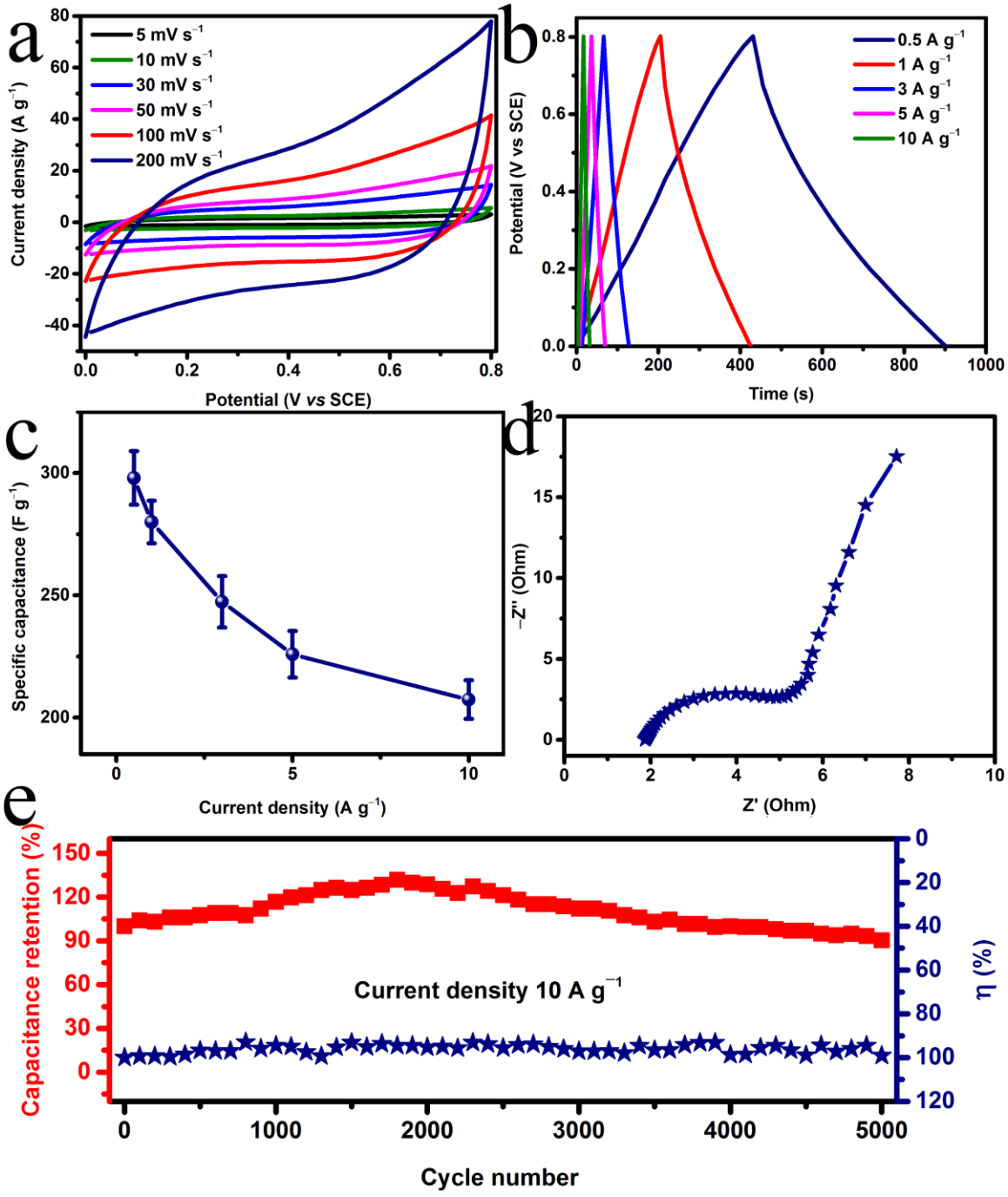

Fig. 4. Three-electrode electrochemical measurements of the GCM in 1M Na_2SO_4 aqueous solution. (a) CV curves at different scans; (b) GCD at various current densities; (c) Specific capacitance of GCM at different current densities; (d) Nyquist plot; (e) Cycling stability performance and Coulombic efficiency.

The GCM film was directly used as a freestanding electrode to evaluate its electrochemical performance in a three-electrode system with 1 M Na_2SO_4 solution as the electrolyte (Fig. 4). The representative CV curves of the GCM electrode at various scan rates ranging from 5–200 mV s^{-1} in a potential window of 0–0.8 V are presented in Fig. 4a. The fast charge/discharge capability of MnO_2 was based on the surface adsorption of the electrolyte cation Na^+, as well as proton incorporation, following the reaction [36]:

$$MnO_2 + xNa^+ + yH^+ + (x+y)e^- \leftrightarrow MnOONa_xH_y \quad (3)$$

The CV curves showed symmetric quasi-rectangular shapes, indicating typical capacitor-like behavior. Smooth CV curves, instead of evident redox peaks, were attributed to the successive multiple surface Faradic reactions of MnO_2 that is a pseudo-capacitive charge storage mechanism that is distinct from that of most other metal oxides [36]. Furthermore, when the scan rate increased, the distortion of CV curves is unconspicuous, suggesting a good rate capability. Fig. 4b presents the GCD curves of the GCM film electrode at different current densities ranging from 0.5–10 A g^{-1}. The GCM film electrode showed an ideal capacitive behavior in terms of the linear and symmetric characteristics, reflecting its high and reversible charge storage capacity. According to the discharge time, the specific capacitances are calculated to be 298, 280, 247, 226, and 207 F g^{-1} at the current densities of 0.5, 1, 3, 5, and 10 A g^{-1}, respectively (Fig. 4c). Approximately 69.5%

of the capacitance for the GCM thin film electrode was retained when the current density increased from 0.5 A g^{-1} to 10 A g^{-1}. Impedance measurements were performed for the GCM thin film, as shown in Fig. 4d. The Nyquist plot exhibited a quasi-semicircle over the high frequency range, followed by a linear component in the low-frequency region. At very high frequencies, the intercept at real part (Z′) indicated the combinational series resistance (R_s) of the electrode, the bulk electrolyte, current collectors, and the electrode/current collector contact resistance. The intercept of the GCM thin film electrode was 1.9 Ω. The diameter of the semicircle corresponded to the charge transfer resistance (R_{ct}) at the interface between the electrode material and the electrolyte. The R_{ct} was measured to be 3.2 Ω for the GCM thin film electrode. The straight line in the low frequency region corresponded to the Warburg resistance (Z_w), suggesting a low diffusion resistance of the GCM thin film electrode. The cycling performance of the GCM thin film electrode was evaluated through repeated charge/discharge tests at a current density of 10 A g^{-1} (Fig. 4e). The GCM thin film manifested a high cycling stability and delivered 90.3% of its initial capacitance even after 5000 cycles. The Coulombic efficiency remained at ~100% during the 5000 charge/discharge cycling tests, further demonstrating the high feasibility of the redox process. To our knowledge, this performance is superior to that of many MnO_2 based electrodes to date (Table S1).

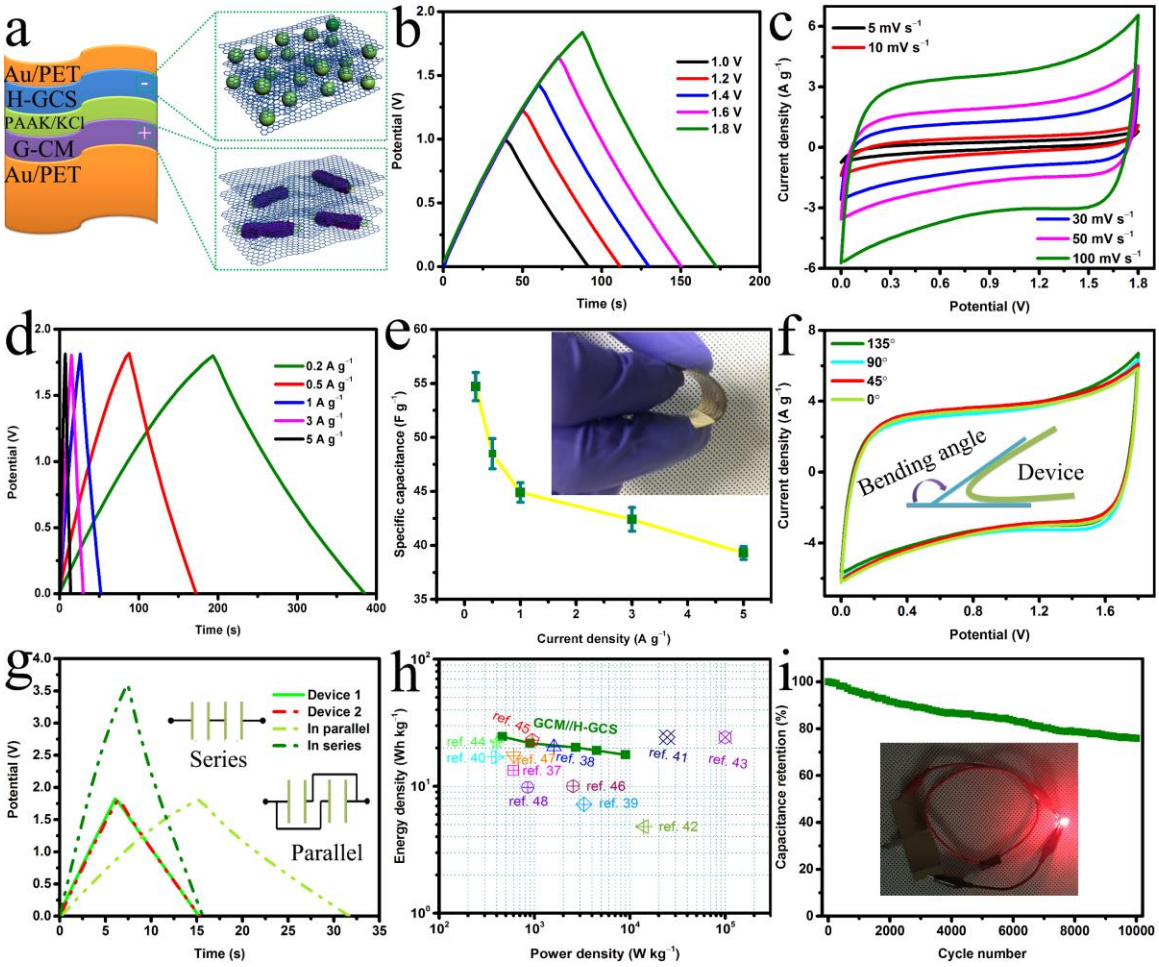

Fig. 5. Electrochemical characterization of the GCM//H-GCS FASC. (a) Scheme of the FASC. (b) GCD curves with the increased potential window. (c) CV curves obtained at different scan rates. (d) GCD curves at various current densities. (e) Specific capacitance at different current densities. Inset: digital image of a bended device. (f) CV curves at different bending angles. (g) GCD of single FASC, and two FASCs in parallel and in series. Inset: schematic circuit diagram of two single FASCs connected in parallel and series configuration. (h) Ragone plot. (i) Cycling performance at current density of 10 A g^{-1}. Inset: red LED powered by two FASCs connected in series.

A FASC with a PAAK/KCl gel electrolyte was assembled using the GCM thin film electrode as the cathode, the H-GCS film electrode as the anode (Fig. 5a). SEM and TEM characterization of H-GCS can be found in Fig. S5 and Fig. S6. The electrochemical performance of the H-GCS electrode was investigated in the three-electrode measurement using 1 M $NaSO_4$ electrode (Fig. S7). The electrochemical behavior of the flexible device was studied thoroughly. The charge/discharge curves of the as-fabricated device at a current density of 5 A g^{-1} remained symmetric at an operating voltage as high as 1.8 V (Fig. 5b), indicating that the device has ideal capacitive behavior with a rapid *I–V* response. Fig. 5c presents the typical CV curves of the flexible device at various scan rates from 5–100 mV s^{-1} between 0–1.8 V. The current density increased as the scan rate increased, and all the CV curves showed a similar shape. The rectangular-like shape and symmetry of the CV scans were well maintained at a high scan rate of 100 mV s^{-1}, indicating the excellent and fast charge/discharge properties and stable electrochemical capacitive characteristics of the device. A GCD test was performed with different current densities over the voltage window of 0–1.8 V, as shown in Fig. 5d. The linear slopes, the triangle shape, and the quick *I-V* response represented the excellent electrochemical reversibility capacitive characteristic that was consistent with the CV curves. The capacitance values of the devices as a function of current density are shown in Fig. 5e. A high specific capacitance of 55 F g^{-1} based on the total mass of the two electrodes can be achieved at 0.2 A g^{-1}. Moreover, it retained 71.9% of its capacitance when the current density was increased from 0.2–5 A g^{-1}, indicating a decent rate capability. The extension of working window and prolonged discharging time could be achieved by constructing tandem SCs, in which single cells were connected in series or in parallel (Fig. 5f). Two

devices connected in series offer a broader, reversible working window up to 3.6 V versus 1.8 V for a single device. Two devices connected in parallel boost the output current by a factor of two over a single device while maintaining a reversible capacitive behavior within a 1.8 V window. To test the flexibility of the device, CV tests were conducted under various bending angles (Fig. 5g). The CV curves showed capacitive behaviors when the bending angle changed from 0° to 135°, displaying excellent device flexibility and stability. The energy and power densities of the device were calculated from the GCD curves and plotted on a Ragone diagram, as shown in Fig. 5h. The maximum gravimetric energy density of 24.6 Wh kg^{-1} (with a power density of 459.3 W kg^{-1}) and power density of 9005.3 W kg^{-1} (with energy density of 17.7 Wh kg^{-1}) were achieved by our flexible device with an operating potential of 1.8 V. These values are superior to previously reported the MnO_2-based asymmetric supercapacitors, such as MnO_2/CNTs//activated carbon (13.3 Wh kg^{-1} at 600 W kg^{-1}) [37], MnO_2/CNTs//porous carbon (20.44 Wh kg^{-1} at 1600 W kg^{-1}) [38], MnO_2/CNTs// MnO_2/CNTs (7.2 Wh kg^{-1} at 3300 W kg^{-1}) [39], ZnO@MnO_2//activated carbon (17 Wh kg^{-1} at 393 W kg^{-1}) [40], graphene/MnO_2//graphene (24.3 Wh kg^{-1} at 24500 W kg^{-1}) [41], carbon particles/MnO_2// carbon particles/MnO_2 (4.8 Wh kg^{-1} at 14000 W kg^{-1}) [42], graphene/MnO_2/carbon black// graphene/carbon black (24.3 Wh kg^{-1} at 10000 W kg^{-1}) [43], MnO_2@carbon fiber//MnO_2@carbon fiber (22.2 Wh kg^{-1} at 400 W kg^{-1}) [44], MnO_x//graphene (23.02 Wh kg^{-1} at 947.11 W kg^{-1}) [45], graphene/MnO_2//graphene (10.03 Wh kg^{-1} at 2530 W kg^{-1}) [46], MnO_2//activated carbon (17.3 Wh kg^{-1} at 605 W kg^{-1}) [47], and MnO_2/conductive polymer// conductive polymer (9.8 Wh kg^{-1} at 850 W kg^{-1}) [48]. The cycling stability of the device was investigated using GCD measurements at a constant

current density of 10 A g^{-1} for 10 000 cycles (Fig. 5i). The as-fabricated device can retain 75.9% of its original capacitance after 10 000 cycles, indicating excellent cycling stability and reliability of the device. As a demonstration for practical application, a red light-emitting (LED) was lit up using two FASCs connected in series (inset in Fig. 5i).

4. Conclusion

In summary, 3D architectures consisting of MnO_2 nanosheets, CNTs, and rGO nanosheets were fabricated. The MnO_2 nanosheets were grafted vertically on CNTs to form a core-shell structure via a secondary (seeded) growth procedure. CM was then encapsulated within rGO nanosheets through a simple vacuum filtration to yield the ternary hybrid GCM film. When evaluated for supercapacitor properties in a three-electrode system, the 3D architecture exhibited high specific capacitance (298 F g^{-1} at 0.5 A g^{-1} and 207 F g^{-1} at 10 A g^{-1}) and excellent cycling stability (90.3% retention after 5000 cycles), which can be attributed to the high utilization of active materials and rapid charge transport in the electrode. Then, the FASC was assembled using 3D GCM and 3D H-GCS films as positive and negative electrodes, respectively, and PAAK-KCl gel as the solid-state electrolyte. The assembled device showed good flexibility, high specific energy density (24.6 Wh kg^{-1} at 459.3 W kg^{-1}), and reasonable cycling performance (75.9% after 10 000 cycles), which is qualified for a promising candidate for the next-generation flexible energy storage devices.

References

[1] G.P. Wang, L. Zhang, J.J. Zhang, A Review of electrode materials for electrochemical supercapacitors, Chem. Soc. Rev. 41 (2012) 797-828.

[2] B. Wei, L.D. Wang, Q.H. Miao, Y.N. Yuan, P. Dong, R. Vajtai, W.D. Fei, Fabrication of manganese oxide/three-dimensional reduced graphene oxide composites as the supercapacitors by a reverse microemulsion method, Carbon 85 (2015) 249-260.

[3] P. Simon, Y. Gogotsi, B. Dunn, Where do batteries end and supercapacitors begin? Science, 343 (2014) 1210-1211.

[4] T. Brousse, D. Bélanger, J.W. Long, To be or not to be pseudocapacitive?, J. Electrochem. Soc. 162 (2015) A5185-A5189.

[5] C.C. Hu, K.H. Chang, M.C. Lin, Y.T. Wu, Design and tailoring of the nanotubular arrayed architecture of hydrous RuO_2 for next generation supercapacitors, Nano. Lett. 6 (2006) 2690-2695.

[6] H.Y. Lee, J.B. Goodenough, Supercapacitor behavior with KCl electrolyte, J. Solid State Chem. 144 (1999) 220-223.

[7] W.J. Ma, S.H. Chen, S.Y. Yang, W.P. Chen, W. Weng, Y.H. Cheng, M.F. Zhu, Flexible all-solid-state asymmetric supercapacitor based on transition metal oxide nanorods/reduced graphene oxide hybrid fibers with high energy density, Carbon 113 (2017) 151-158.

[8] M. Toupin, T. Brousse, D. Belanger, Charge storage mechanism of MnO_2 electrode used in aqueous electrochemical capacitor , Chem. Mater. 16 (2004) 3184-3190.

[9] X.L. Wang, X.Y. Fan, G. Li, M. Li, X.C. Xiao, A.P. Yu, Z.W. Chen, Composites of MnO_2 nanocrystals and partially graphitized hierarchically porous carbon spheres with

improved rate capability for high-performance supercapacitors, Carbon 93 (2015) 258-265.

[10] Y.B. Zhang, B. Wang, F. Liu, J.P. Cheng, X.W. Zhang, L. Zhang, Full synergistic contribution of electrodeposited three-dimensional $NiCo_2O_4$@MnO_2 nanosheet networks electrode for asymmetric supercapacitors, Nano Energy 27 (2016) 627-637.

[11] J.L. Kang, A. Hirata, L.J. Kang, X.M. Zhang, Y. Hou, L.Y. Chen, C. Li, T. Fujita, K. Akagi, M.W. Chen, Enhanced supercapacitor performance of MnO_2 by atomic doping, Angew. Chem. Int. Edit. 52 (2013) 1664-1667.

[12] R.H. Baughman, A.A. Zakhidov, W.A. de Heer, Carbon nanotubes - the route toward applications, Science 297 (2002) 787-792.

[13] T. Lv, Y. Yao, N. Li, T. Chen, Highly stretchable supercapacitors based on aligned carbon nanotube/molybdenum disulfide composites, Angew. Chem. Int. Edit. 55 (2016) 9191-9195.

[14] X. Xiao, T.Q. Li, P.H. Yang, Y. Gao, H.Y. Jin, W.J. Ni, W.H. Zhan, X.H. Zhang, Y.Z. Cao, J.W. Zhong, L. Gong, W.C. Yen, W.J. Mai, J. Chen, K.F. Huo, Y.L. Chueh, Z.L. Wang, J. Zhou, Fiber-based all-solid-state flexible supercapacitors for self-powered systems, Acs Nano 6 (2012) 9200-9206.

[15] C. Choi, J.A. Lee, A.Y. Choi, Y.T. Kim, X. Lepro, M.D. Lima, R.H. Baughman, S.J. Kim, Flexible supercapacitor made of carbon nanotube yarn with internal pores, Adv. Mater. 26 (2014) 2059-2065.

[16] S.X. Wu, K. San Hui, K.N. Hui, J.M. Yun, K.H. Kim, A novel approach to fabricate carbon-sphere-intercalated holey graphene electrode for high-energy-density electrochemical capacitors, Chem. Eng. J. 317 (2017) 461-470.

[17] Hummers, W. S.; Offeman, R. E., Preparation of graphitic oxide. J. Am. Chem. Soc. *80* (1958) 1339.

[18] N.I. Kovtyukhova, P.J. Ollivier, B.R. Martin, T.E. Mallouk, S.A. Chizhik, E.V. Buzaneva, A.D. Gorchinskiy, Layer-by-layer assembly of ultrathin composite films from micron-sized graphite oxide sheets and polycations, Chem. Mater. 11 (1999) 771-778.

[19] D. Li, M.B. Muller, S. Gilje, R.B. Kaner, G.G. Wallace, Processable aqueous dispersions of graphene nanosheets, Nat. Nanotechnol. 3 (2008) 101-105.

[20] X.M. Sun, Y.D. Li, Colloidal carbon spheres and their core/shell structures with noble-metal nanoparticles, Angew. Chem. Int. Edit. 43(5) (2004) 597-601.

[21] Z.Y. Zhang, F. Xiao, L.H. Qian, J.W. Xiao, S. Wang, Y.Q. Liu, Facile synthesis of 3D MnO_2-graphene and carbon nanotube-graphene composite networks for high-performance, flexible, all-solid-state asymmetric supercapacitors, Adv. Energy Mater. 4 (2014).

[22] X. Jin, W. Zhou, S. Zhang, G.Z. Chen, Nanoscale microelectrochemical cells on carbon nanotubes, Small 3 (2007) 1513-1517.

[23] M.S.P. Shaffer, X. Fan, A.H. Windle, Dispersion and packing of carbon nanotubes, Carbon 36 (1998) 1603-1612.

[24] D. Yan, P.X. Yan, S. Cheng, J.T. Chen, R.F. Zhuo, J.J. Feng, G.A. Zhang, Fabrication, in-depth characterization, and formation mechanism of crystalline porous birnessite MnO_2 film with amorphous bottom layers by hydrothermal method, Cryst. Growth Des. 9 (2009) 218-222.

[25] R.J. Chen, P. Zavalij, M.S. Whittingham, Hydrothermal synthesis and characterization of $K_xMnO_2 \cdot yH_2O$, Chem. Mater. 8 (1996) 1275-1280.

[26] F.Z. Zhang, L. Guo, S.L. Xu, R. Zhang, Preparation of nickel-aluminum-containing layered double hydroxide films by secondary (seeded) growth method and their electrochemical properties, Langmuir 31 (2015) 6704-6712.

[27] D. Yan, P.X. Yan, G.H. Yue, J.Z. Liu, J.B. Chang, Q. Yang, D.M. Qu, Z.R. Geng, J.T. Chen, G.A. Zhang, R.F. Zhuo, Self-assembled flower-like hierarchical spheres and nanobelts of manganese oxide by hydrothermal method and morphology control of them, Chem. Phys. Lett. 440 (2007) 134-138.

[28] A.L.M. Reddy, M.M. Shaijumon, S.R. Gowda, P.M. Ajayan, Coaxial MnO_2/carbon nanotube array electrodes for high-performance lithium batteries, Nano Lett. 9 (2009) 1002-1006.

[29] S.X. Wu, K.S. Hui, K.N. Hui, One-dimensional core-shell architecture composed of silver nanowire@hierarchical nickel-aluminum layered double hydroxide nanosheet as advanced electrode materials for pseudocapacitor, J. Phys. Chem. C 119 (2015) 23358-23365.

[30] D. Pandey, R. Reifenberger, R. Piner, Scanning probe microscopy study of exfoliated oxidized graphene sheets, Surf. Sci. 602 (2008) 1607-1613.

[31] T. Szabo, O. Berkesi, P. Forgo, K. Josepovits, Y. Sanakis, D. Petridis, I. Dekany, Evolution of surface functional groups in a series of progressively oxidized graphite oxides, Chem. Mater. 18 (2006) 2740-2749.

[32] Y.C. Chen, H. Ishihara, W.J. Chen, N. DeMarco, A. Siordia, Y.S. Sun, O. Lin, C.W. Chu, V.C. Tung, Capillarity-assisted electrostatic assembly of hierarchically functional 3D graphene: TiO_2 hybrid photoanodes, Adv. Mater. Interfaces 2 (2015)1500292.

[33] S.X. Wu, K.S. Hui, K.N. Hui, K.H. Kim, Electrostatic-induced assembly of graphene-encapsulated carbon@nickel-aluminum layered double hydroxide core-shell spheres hybrid structure for high-energy and high-power-density asymmetric supercapacitor, Acs Appl. Mater. Inter. 9 (2017) 1395-1406.

[34] J.H. Lee, N. Park, B.G. Kim, D.S. Jung, K. Im, J. Hur, J.W. Choi, Restacking-inhibited 3D reduced graphene oxide for high performance supercapacitor electrodes, Acs Nano 7 (2013) 9366-9374.

[35] H.B. Feng, R. Cheng, X. Zhao, X.F. Duan, J.H. Li, A low-temperature method to produce highly reduced graphene coxide, Nat. Commun. 4 (2013) 1539.

[36] P. Simon, Y. Gogotsi, Materials for electrochemical capacitors, Nat. Mater. 7 (2008) 845-854.

[37] L. Li, Z.A. Hu, N. An, Y.Y. Yang, Z.M. Li, H.Y. Wu, Facile synthesis of MnO_2/CNTs composite for supercapacitor electrodes with long cycle stability, J. Phys. Chem. C 118 (2014) 22865-22872.

[38] R.R. Salunkhe, H. Ahn, J.H. Kim, Y. Yamauchi, Rational design of coaxial structured carbon nanotube-manganese oxide (CNT-MnO_2) for energy storage application, Nanotechnology 26 (2015) 204004.

[39] W.Y. Ko, Y.F. Chen, K.M. Lu, K.J. Lin, Porous honeycomb structures formed from interconnected MnO_2 sheets on CNT-coated substrates for flexible all-solid-state supercapacitors, Sci. Rep. 6 (2016) 18887.

[40] A.V. Radhamani, K.M. Shareef, M.S.R. Rao, ZnO@MnO_2 core-shell nanofiber cathodes for high performance asymmetric supercapacitors, Acs Appl. Mater. Inter. 8 (2016) 30531-30542.

[41] X. Zhao, L.L. Zhang, S. Murali, M.D. Stoller, Q.H. Zhang, Y.W. Zhu, R.S. Ruoff, Incorporation of manganese dioxide within ultraporous activated graphene for high-performance electrochemical capacitors, Acs Nano 6 (2012) 5404-5412.

[42] L.Y. Yuan, X.H. Lu, X. Xiao, T. Zhai, J.J. Dai, F.C. Zhang, B. Hu, X. Wang, L. Gong, J. Chen, C.G. Hu, Y.X. Tong, J. Zhou, Z.L. Wang, Flexible solid-state supercapacitors based on carbon nanoparticles/MnO_2 nanorods hybrid structure, Acs Nano 6 (2012) 656-661.

[43] J.C. Chen, Y.M. Wang, J.Y. Cao, Y. Liu, J.H. Ouyang, D.C. Jia, Y. Zhou, Flexible and solid-State asymmetric supercapacitor based on ternary graphene/MnO_2/carbon black hybrid film with high power performance, Electrochim. Acta 182 (2015) 861-870.

[44] D.Y. Zhang, Y.H. Zhang, Y.S. Luo, P.K. Chu, Highly porous honeycomb manganese oxide@carbon fibers core-shell nanocables for flexible supercapacitors, Nano Energy 13 (2015) 47-57.

[45] J. Yang, G.Z. Li, Z.H. Pan, M.N. Liu, Y. Hou, Y.J. Xu, H. Deng, L.M. Sheng, X.L. Zhao, Y.C. Qiu, Y.G. Zhang, All-solid-state high-energy asymmetric supercapacitors enabled by three-dimensional mixed-valent MnO_x nanospike and graphene electrodes, Acs Appl. Mater. Inter. 7 (2015) 22172-22180.

[46] L.J. Deng, G. Zhu, J.F. Wang, L.P. Kang, Z.H. Liu, Z.P. Yang, Z.L. Wang, Graphene-MnO_2 and graphene asymmetrical electrochemical capacitor with a high energy density in aqueous electrolyte, J. Power Sources 196 (2011) 10782-10787.

[47] T. Cottineau, M. Toupin, T. Delahaye, T. Brousse, D. Belanger, Nanostructured transition metal oxides for aqueous hybrid electrochemical supercapacitors, Appl. Phys. A-Mater. 82 (2006) 599-606.

[48] J. Duay, E. Gillette, R. Liu, S.B. Lee, Highly flexible pseudocapacitor based on freestanding heterogeneous MnO_2/conductive polymer nanowire arrays, Phys. Chem. Chem. Phys. 14 (2012) 3329-3337.